Metals & corrosion

Unveiling the microstructure evolution and mechanical properties in a gas tungsten arc-welded Fe–Mn–Si–Cr–Ni shape memory alloy

J. G. Lopes[1,2,3,*], D. Martins[3], K. Zhang[2], B. Li[4], B. Wang[5], X. Wang[6], N. Schell[7], E. Ghafoori[8], A. C. Baptista[3], and J. P. Oliveira[1,3,*]

[1] UNIDEMI, Department of Mechanical and Industrial Engineering, NOVA School of Science and Technology, Universidade NOVA de Lisboa, 2829-516 Caparica, Portugal

[2] Centre for Advanced Materials Joining, Department of Mechanical and Mechatronics Engineering, University of Waterloo, 200 University Avenue West, Waterloo, ON N2L 3G1, Canada

[3] CENIMAT/I3N, Department of Materials Science, NOVA School of Science and Technology, Universidade NOVA de Lisboa, 2829-516 Caparica, Portugal

[4] Western Superconducting Technologies Co., Ltd., Shaanxi Province Engineering Laboratory for Aerial Material, Xi'an 710018, China

[5] National Key Laboratory for Precision Hot Processing of Metals, School of Materials Science and Engineering, Harbin Institute of Technology, Harbin 150001, China

[6] Canadian Centre for Electron Microscopy, McMaster University, Hamilton, ON L8S 4M1, Canada

[7] Institute of Materials Physics, Helmholtz-Zentrum Hereon, Max-Planck-Str. 1, 21502 Geesthacht, Germany

[8] Institute for Steel Construction, Faculty of Civil Engineering and Geodetic Science, Leibniz University Hannover, 30167 Hannover, Germany

ABSTRACT

Fe–Mn–Si–Cr–Ni shape memory alloys (SMAs) are unique low-cost materials with shape memory properties that grant them the ability to be used in both functional and structural applications. Such SMAs are especially sought in the construction sector for the creation of new components and/or the reinforcement of damaged ones. In this study, a Fe–17Mn–5Si–10Cr–4Ni–1(V, C) wt% SMA was gas tungsten arc welded, with the objective to investigate the microstructure and mechanical performance changes occurring after welding. A comprehensive assessment of processing, microstructure and properties relationships was established combining microscopy (optical and electron), synchrotron X-ray diffraction, microhardness mapping and tensile testing including cycling assessment of the joint's functional performance. It is shown that the present SMA has good weldability, with the joints reaching nearly 883 MPa at fracture strain of $23.6 \pm 2.1\%$. Alongside this, several microstructure differences were encountered between the as-received and as-welded condition, including the formation of ferrite and $Fe_5Ni_3Si_2$ $P2_13$ cubic precipitates amidst the fusion zone in the latter region.

Handling Editor: Zhao Shen.

Address correspondence to E-mail: jcg.lopes@campus.fct.unl.pt; jp.oliveira@fct.unl.pt

🍃 Springer

GRAPHICAL ABSTRACT
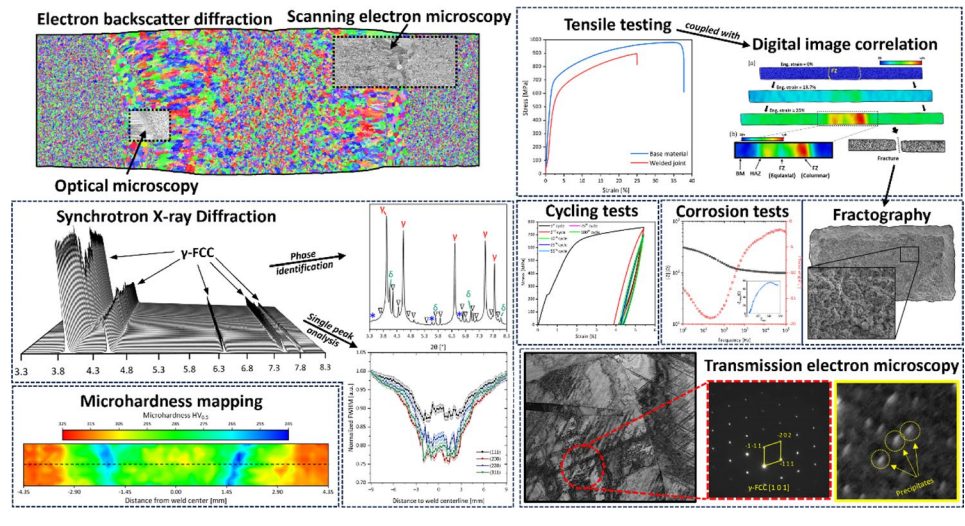
Introduction

Fe–Mn–Si-based shape memory alloys (SMAs) are promising advanced materials with a strong potential for structural engineering purposes. While these alloys can be manufactured by similar methods as those of conventional steels, their unique ability for exhibiting the shape memory effect, makes them particularly interesting for engineering applications within the construction sector. These range from fabrication of pre-stressed reinforcements [1–4], tube couplings [5], actuators [6, 7], and the strengthening of damaged structures [8, 9].

Belonging to the SMA class of metals, the shape memory effect, which is intrinsic to these materials, grants them the ability to recover to their original condition after prior deformation, followed by an imposed thermal stimulus. Such effect is attained due to a reversible phase transformation process. In other terms, the shape memory effect for these materials can be explained as follows: First, by exposing the alloy to external stresses, the transformation of an austenitic phase (γ-FCC), which is stable at high temperatures, to a martensitic phase (ε-HCP), which is stable at low temperatures, is triggered. However, upon temperature increase up to the austenitic domain, the reverse transformation occurs, where the SMA, now composed by mixture of γ-FCC and ε-HCP, will transform

back into γ-FCC prevalent microstructure, thus causing the material to return to its original shape [9, 10].

Given their outstanding potential, the study on their processability is fundamental to expand the potential scope of applications associated with these materials. This allows for the optimization of manufacturing costs and quality control factors, granted that their microstructure and mechanical performance is considered during the component design phase. In the realm of the welding process, gas tungsten arc welding (GTAW) is based on the premise of using a non-consumable tungsten electrode, shielded by an inert gas, to permanently join two (or more) components. The main advantages of GTAW include its low cost and good precision, being applicable to most joint configurations, effectively making it a widely used technique in a vast array of industries [9, 11]. However, due to the high temperatures generated in the process there is local material melting, where upon its solidification a microstructural discontinuity is generated. Such factor can be aggravated by the nucleation of intermetallic compounds within the joint, as well as cracks and residual stresses in the solidified material [9, 12–14].

Regarding the study on the welding of Fe–Mn–Si-based SMAs, Druker et al. [5] investigated the formability and weldability of Fe–15Mn–5Si–9Cr–5Ni sheets using GTAW to observe how this welding process

affected the mechanical and shape memory properties. Their results indicated that the GTAW influences both the mechanical and shape memory properties of the alloy, negatively impacting them. Furthermore, direct observations under synchrotron X-ray light were performed by Nagira et al. [15] during single spot GTAW, on both Fe–15Mn–10Cr–8Ni–4Si and Fe–15Mn–11Cr–7.5Ni–4Si alloys. Their efforts allowed them to observe how the solidification mode influenced the solidification cracking susceptibility of the molten pool. Beyond these other studies detailed that an effort is being made to study the weldability of these alloys, especially when using laser-based technologies [16, 17].

This work aims to delve deeper into the microstructure and mechanical property assessment of a gas tungsten arc welded Fe–17Mn–5Si–10Cr–4Ni–1(V, C) wt% SMA, using both conventional and advanced characterization techniques. Firstly, microstructural assessment is performed by optical, scanning and transmission electron microscopy techniques, followed by synchrotron X-ray diffraction analysis across the welded joint. Secondly, the mechanical performance of the weld is studied via microhardness mapping, tensile testing, coupled with digital image-correlation. Additional cyclic load/unloading tests are performed, detailing the correlation between processing conditions, microstructure features and property variation.

Materials and methods

In this study, a Fe–17Mn–5Si–10Cr–4Ni–1(V, C) wt% shape memory alloy was used as base material (BM), where VC precipitation has been recognized as a promoter of the superelastic effect [9, 18]. Before GTAW, the base material underwent hot-rolling (at 1000 °C) until reaching a thickness of 3 mm, followed by subsequent cold-rolling to achieve a final thickness of 1.5 mm. Rectangular-shaped coupons, with dimensions of 30 × 60 mm, were then cut from the 1.5 mm plates, and cleaned with alcohol and acetone prior to welding.

The coupons were butt welded using an in-house developed CNC 3-axis machine to control the speed and torch position. The torch was connected to an OERLIKON CITOTIG 2200 FORCE source. GTAW was conducted using direct current with an intensity of 110 A and a welding speed of 60 mm/min, to guarantee full penetration. Argon shielding gas was utilized to protect the molten pool and surrounding heat affected zone, at a flow rate of 8 L/min coming from the torch and 5 L/min coming from the fixture. The tip of the tungsten electrode was kept at a fixed distance of 1.5 mm from the plate. This choice of parameters implied a heat input of 1.6 kJ/mm to be applied during welding.

Standard metallographic preparation was then applied to subsequently evaluate the microstructure across the joint. Here, the joint cross section was cold mounted and mechanically polished with progressively finer silicon carbide sandpapers. Final polishing was conducted using 3 μm diamond paste until a surface-mirror like aspect was obtained. Etching was then performed using a mixture of ethanol, hydrochloric acid and nitric acid in a 17:2:1 in volume. To inspect the microstructure, optical microscopy was performed on a Leica DMI5000 M inverted optical microscope. Furthermore, scanning electron microscopy (SEM) was also conducted using a Hitachi SU3800. EBSD (electron backscattered diffraction) analysis was conducted on a Zeiss SUPRA55 SEM and subsequent processing of the raw data was performed using in-house developed MATLAB routines. Nanoscale characterization was conducted via in Talos L120C and Talos 200X analytical transmission electron microscope (TEM) and scanning electron microscope (STEM) equipped with energy dispersive X-ray spectroscopy (EDS) operation at 120 keV and 200 keV, scanning transmission electron microscopy (TEM) and scanning TEM (STEM) operating at 200 kV respectively. The specific-sites of TEM lamellas from base material (BM) and fusion zone (FZ) areas were prepared by the plan-view lift out method in a Helios 5 plasma focused ion beam (PFIB).

High energy synchrotron X-ray diffraction was performed on the P07 beamline in PETRAIII/DESY, Germany. There, the material was exposed to an X-ray beam with a wavelength of 0.14235 Å, corresponding to an energy of 87.1 keV, to obtain crystallographic-dependent microstructure information throughout the joint. The beam size was set at 200 × 200 μm², and the joint was probed from one side of the BM to the opposite side with steps of 200 μm. The distance from the detector to the material was 1364 mm. A 2D Perkin Elmer XRD 1622 fast detector was used to capture the Debye–Scherrer rings. The raw data was then integrated using DIOPTAS software, allowing to identify the existing phases across the welded joint.

Additionally, single peak fitting was performed to obtain information on microstrain and peak intensity evolution throughout the welded joint. Such analysis was complemented using GSAS II software [19].

Electrochemical characterization was performed in a conventional three-electrode setup using a potentiostat/galvanostat Interface 1010 from Gamry Instruments. For this, samples were taken from the BM and the FZ, which served as the working electrode, while a platinum wire acted as the counter electrode. A Ag/AgCl reference electrode was utilized as the reference electrode. The samples were immersed in a 3.5 wt.% NaCl electrolyte solution for 2 h to establish a steady state of the open circuit potential (OCP). Potentiodynamic polarization measurements were immediately conducted at a scan rate of 1 mV/s in the voltage range from − 1.5 to 1.5 V. Electrochemical impedance spectroscopy (EIS) measurements were subsequently performed on these samples across a frequency range from 1 Hz to 100 kHz.

To further understand the mechanical properties after welding and to correlate them with the observed microstructure and processing conditions, microhardness mapping using a Mitutoyo HM-112 hardness tester was conducted on the full extent of the cross-section. Each indentation was imposed with a load of 500 g applied for 10 s, and was spaced 150 μm apart from the surrounding indentations. Furthermore, tensile tests were carried out at room temperature until fracture, using an Autograph Shimadzu AG-50kNG machine, with a displacement rate of 1 mm/min. During tensile testing, tests were recorded and subsequently analyzed using digital image correlation (DIC). The fractured surfaces were observed via SEM. Finally, cycling load/unload tests, limited to a maximum imposed strain of 6% followed by unloading to a stress-free condition, were performed to a total of 100 cycles.

Results and discussion

Microstructure analysis of the welded joint

To fully assess the effect of GTAW on the Fe–Mn–Si–Cr–Ni SMA, it is important to characterize the resulting welded joint considering both microstructural and mechanical aspects. This paves the way to establish connections between each other, and consequently generating a more precise understanding on

the processing-microstructure-properties relationships for this material/welding process pair combination. In this section standard and advanced characterization techniques are employed to investigate the microstructure encountered on the cross-section of the weld with the purpose of correlating it with the mechanical behavior exhibited by the welded joint.

Optical and scanning electron microscopy

Commencing by the microstructure assessment, Fig. 1a displays a representative cross-section of the welded sample. Here, clear microstructural differences between the BM and the fusion zone (FZ) are evidenced. That is, while the BM is composed
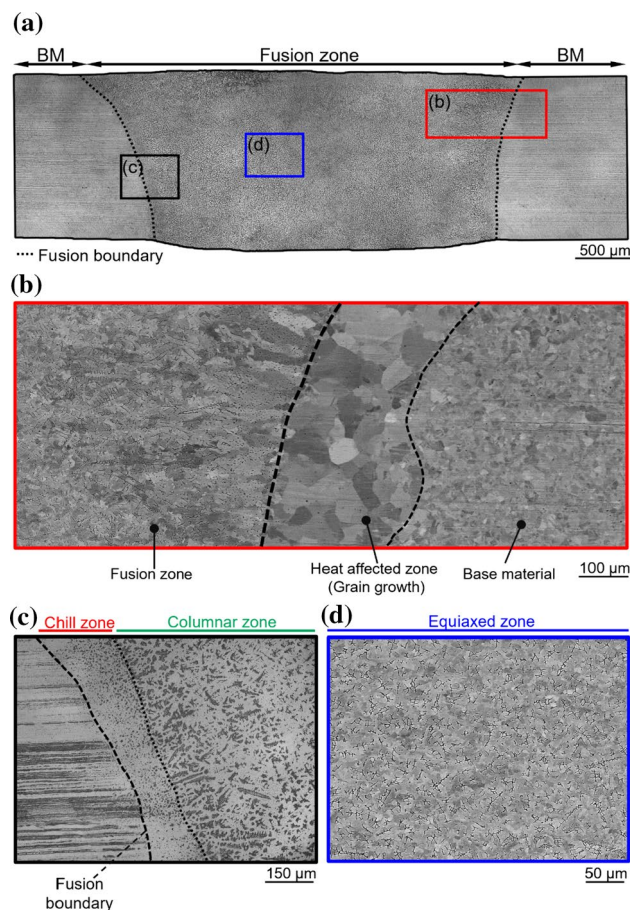

Figure 1 Microstructural analysis of the welded joint: **a** Overview of the joint as obtained by optical microcopy; **b** Scanning electron microscopy of the transition from the BM to the FZ highlighting the several regions generated during welding; **c** Close-up view of the transition from the BM to the FZ by optical microscopy; **d** Close-up view of the FZ by SEM.

mainly of small equiaxed grains, with a grain size of 11.4 ± 3.0 μm, the FZ presents itself as a plethora of grain morphologies that formed upon the non-equilibrium cooling conditions experienced by the molten pool. Nevertheless, before a detailed analysis of FZ is provided, understanding the microstructural changes that occurred throughout all the regions that comprise the weld must be done.

For this we refer to Fig. 1b, where a SEM image taken using a backscattered electrons (BSE) detector reveals the microstructural variations that occurred near the fusion boundary (FB). The FB encompasses both the heat affected zone (HAZ), where the material did not experience full melting, and the FZ, where complete melting occurred. The HAZ is characterized by the potential occurrence of solid-state transformations that alter the original BM microstructure. Here, recovery, recrystallization and grain growth can occur, although the extent of these transformations will be dependent on both the distance to the heat source, which impacts the local thermal cycle, and the previous thermomechanical processing of the BM, which will influence the magnitude of the eventual solid state transformations that can occur. Evidence of grain growth in the HAZ is clearly observed in Fig. 1b, where the average grain size is 42.2 ± 8.7 μm, while in the BM this value was solely of 11.4 ± 3.0 μm.

When crossing the FB, the FZ is reached, a variety of grain structures of different sizes and morphologies are observed. Here, the optical micrographs of Fig. 1c and d clearly display regions that are commonly identified from solidification theory: the chill, columnar and equiaxed zones. In welding-related literature, however, evidence of small equiaxed grains at the FZ boundary is often referred to as fine equiaxed zone (FQZ), being commonly found in Al alloys, for example, and can be a weak point in the joint [20, 21]. Nevertheless, in this study we refer to it as the chill zone to maintain the consistency with the classical metallurgical theory of solidifying ingots, allowing us to make the parallel between the fundamental knowledge of solidification and the microstructures possible to obtain during GTAW. Thus, the chill zone presents itself as a region comprising small and tightly packed equiaxed grains with an average size of 9.9 ± 2.1 μm. Further into the FZ, the columnar zone is formed, and this region is composed of highly directional columnar dendrites that grow epitaxially from the grains formed in the chill zone. Measured along their growth direction these grains reach 107.9 ± 20.0 μm. Their high

directionality is due to the competitive growth that occurs, as grains tend to follow the path for maximum heat extraction, growing as the cooling rate decreases due to their proximity to the center of the FZ, where the process peak temperature is attained. Lastly, in the core of the FZ, an equiaxed zone can be observed with an averaged grain size of 27 ± 6.8 μm. This region is comprised by relatively larger equiaxed dendritic grains that form during dendritic growth, where under the appropriate conditions the dendritic arms can break providing, in the process, new nucleation sites for new and equiaxed dendrites to form, as depicted in Fig. 1d.

Amidst the grain boundaries of the solidified dendrites, which is especially evident in Fig. 1d, the presence of vermicular ferrite (δ-BCC) is also shown. Over the past years, the formation of δ-BCC has been related to the relationship between the Cr_{eq}/Ni_{eq}, material solidification modes [22, 23] and cooling rate [24, 25]. Given this, Peng et al. [23], developed Eq. 1 to help predict the solidification modes of cast Fe–Mn-Si-Cr-Ni SMAs, as follows:

$$\frac{Cr_{eq}}{Ni_{eq}} = \frac{Cr + 1.5\,Si}{Ni + 0.164\,Mn + 22\,C} \qquad (1)$$

Using the nominal composition of the SMA, the Cr_{eq}/Ni_{eq} ratio was calculated to be 0.98, which is below the 1.35 threshold, indicating that the solidification mode of the alloy should follow the sequence: L (Liquid) → L + γ-FCC → γ-FCC. Thus, in the final stages of solidification the material should be fully austenitic. Such is indeed the case of the BM and the HAZ, which did not undertake fully remelting during welding. Nevertheless, the displayed results indicate that the microstructure is not only composed of γ-FCC. To understand how other phases appear on the microstructure, the constitutional supercooling theory allows us to interpret the continuous compositional change that the molten pool undergoes. As the molten metal starts to solidify, small dendritic arms start growing from the already present solid material, which acts as primary solidification sites. With the decrease in temperature, while some atoms arrange themselves in the matrix γ-FCC phase crystal structure, the dendritic boundaries become richer with the remaining elements present in the molten pool, with the continuous decrease in temperature and the consequent solute-rich interdendritic fluid [12]. The remaining atoms will solidify in the crystal structure that has

the lowest Gibbs free energy for such interdendritic fluid composition. In the present case the formation of δ-BCC can be explained by the enrichment of Cr and/or Si via segregation into the molten pool, as these present themselves as factors that can dictate the Cr_{eq} value used to determine the solidification mode of the alloy [23]. Other phases are nonetheless possible to appear in the microstructure, depending on the overall Gibbs free energy of the system at specific sites with determined compositions, as well as cooling and mixing conditions experienced by the material, which are known to vary within the welded joint. Nevertheless, predicting the solidification path that the molten material undergoes during welding is not trivial, as several other factors come into play during the process. Beyond the composition and phase structures enveloped in the microstructure, grain morphology and orientation are also a product of material solidification.

Figure 2 displays the inverse pole figure (IPF) orientation map of the welded joint. Here, the same microstructural features observed via optical microscopy along the weld are also put in evidence alongside a clearer perspective on the grain orientations. Considering Fig. 2b, it is observed that the BM is randomly oriented, then in the HAZ there is evidence of massive grain growth. Crossing the FB, entails the FZ regions which is composed by: (i) the chill zone, containing the small sized grains; (ii) the columnar region, where

grain growth is preferential along the easy growth direction for cubic alloys, i.e., the <100> direction; and (iii) the equiaxed grain regions, where the formed grains are randomly oriented.

Returning to the topic of grain morphologies, which has already been mentioned briefly, Fig. 2a shows a clearer distribution of the grain structures located throughout the several regions of the molten pool. The presence of this microstructural variation in the molten pool, as shown in Fig. 2, arises from the process thermal cycle experienced by the material, which is essentially controlled by the process heat input and material thermophysical properties. The heat input ultimately impacts the overall shape of the weld and, more importantly, has a major impact on the microstructural features of the weld by dictating how the temperature gradient (G) and the growth rate (R) vary along the solidifying molten metal. In this study, the presence of these different grain shapes highlights the varying conditions that reign over the thermal gradient and growth rate that eventually results on the formation of the several regions present in the FZ [12].

The small equiaxed grains that composed the chill zone occur as the combination of an elevated growth rate and a low thermal gradient, compounded by the high cooling rates enabled by the cold BM that then transforms to HAZ due to heat dissipation from the FZ. This will be the first region to solidify, and grains

Figure 2 Electron Backscatter Diffraction Inverse Pole Figure map parallel to the Z axis: **a** cross section of the welded joint; **b** Detailed view of the fusion boundary.
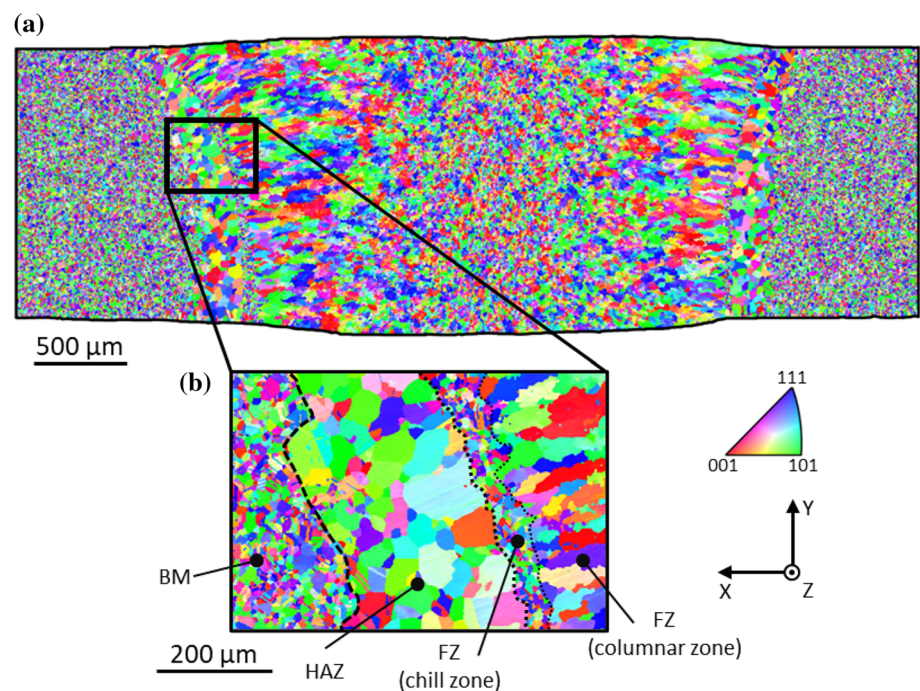
formed here will act as substrates for columnar grains to start growing towards the center of the FZ. The small dimension exhibited by this region, when compared to the remaining regions of the FZ, indicates that the influence of the BM in the temperature distribution is the key factor that reins over the solidification microstructure of the molten pool developed here.

Next, there exists the columnar zone, where dendritic structures grow collectively aligned with the maximum thermal gradient. In this region, the thermal gradient factor increases over the growth rate, thus allowing for the competitive growth showcased by the large dendrites exhibited in this region. Finally, at the center of the FZ, where the equiaxed zone developed, the temperature reaches its maximum values during welding, while the cooling effect induced by the cold BM is reduced due to it being further away, therefore also decreasing the effect of G. In this region other factors such as the fragmentation of dendritic arms, due to their rapid and directional growth combined with the molten pool turbulence, can ease the formation of new dendrites providing new nucleation sites for the

liquid to solidify from, increasing R in the process. Additionally, being so near to the torch, the cooling rate is also slower in this region, thus larger equiaxed grains structures can be observed, when compared to those formed in the chill zone.

Transmission electron microscopy

Beyond the optical and SEM observations made until now, a deeper analysis of the microstructure of the BM and the FZ at the nanoscale was performed using S/TEM. Nanoscale characterization of the BM using TEM is detailed in Fig. 3, where the features present at the sub-grain level are exhibited.

In Fig. 3a it is possible to observe the multiple sets of stacking faults (SFs) within all the grain structures, for example, as marked by the yellow dashed lines. These are characteristics of the previous thermomechanical processing endured by the BM during its manufacturing processing, acting as a method to release energy alongside the possible

Figure 3 **a** representative bright field TEM image of the BM; **b** SAED pattern highlighting the γ-FCC matrix; **c** SAED pattern indicating the presence of an annealing twin alongside the γ-FCC matrix; **d** TEM image detailing the presence of stacking faults within the annealing twin, and **e** SAED pattern of the annealing twin showcasing streaking due to the presence of stacking faults.
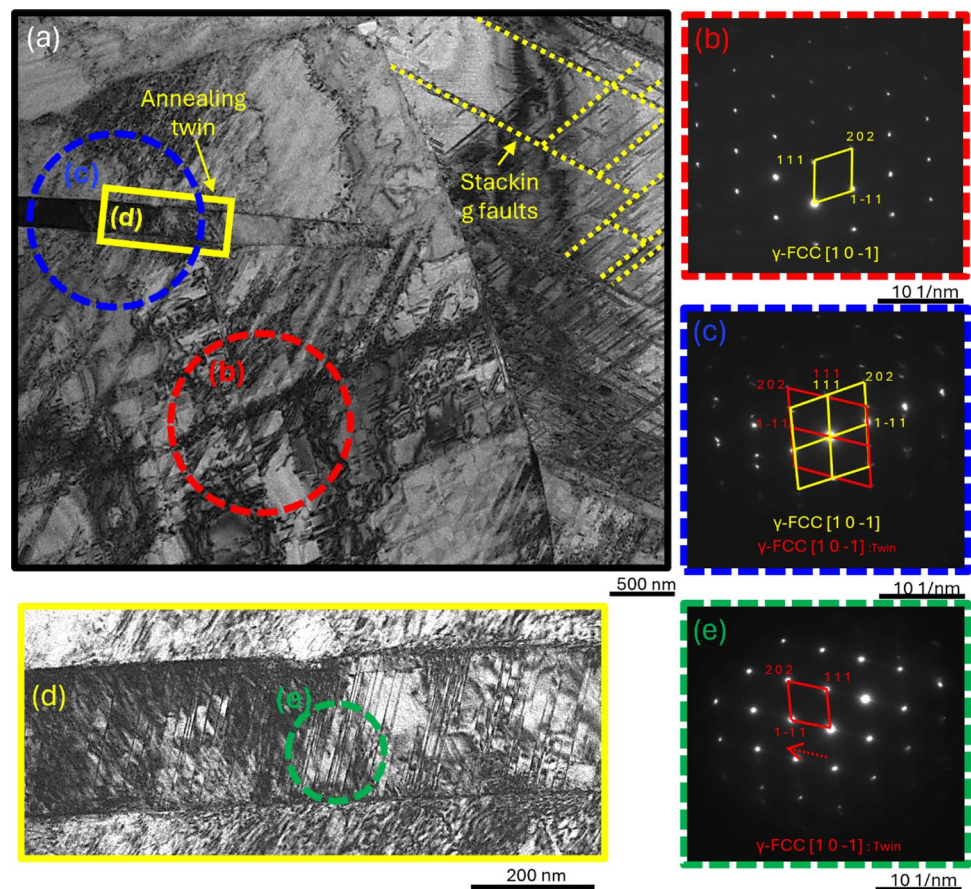
formation of deformation twins. Additionally, a representative selected area electron diffraction (SAED) pattern is depicted in Fig. 3b, showcasing the γ-FCC matrix phase as the only identifiable phase in the microstructure, as no other obvious diffraction spots were noticeable within the analyzed region of the BM.

Emphasis is now given to an annealing twin with a thickness of ≈ 250 nm shown in Fig. 3d. This feature is associated with the thermal influence associated with the hot-rolling endured by the BM, resulting from the recrystallization mechanisms undertaken during the process. The corresponding SAED pattern is displayed in Fig. 3c, where two sets of diffraction pattern spots are evidenced, indicating the misorientation between the annealing twin and the matrix. Interestingly within these twins, the presence of fine SFs can be observed, which are compliant with the extensive streaking along the <111> γ direction, which extends through the γ-FCC matrix reflections and is associated with fine SFs.

Figure 4 depicts a TEM image obtained from the FZ region. Here, larger γ-FCC matrix grains are composed of smaller polygonal sub-grain structures exhibiting a lower density of defects within the γ-FCC matrix, when compared to the BM (see Fig. 3). Additionally, two different types of precipitates are also visible. Firstly, as noticeable in Fig. 4b and c, small particles corresponding to vanadium carbides were distributed near the sub grain boundaries. This was expected to occur in the microstructure given the nominal composition of the alloy. On a second instance it was also possible to identify Fe-rich nanoparticles (refer to Fig. 4d and e) scattered within the grains. An EDS line scan was acquired to further highlight their presence, as shown in Fig. 4f). Phase identification using SAED was not possible to conduct in these particles, given their small size and/or their random orientation on the γ-FCC matrix. The identification of these nanoparticles will be detailed when presenting the high energy synchrotron X-ray diffraction data.

SAED analysis was conducted in the transition between two different sub-grains and their boundary, depicted in Fig. 4g, h and i, the diffraction patterns corresponded to that of the γ-FCC matrix phase. Interestingly, a small disorientation angle, indicating a low angle boundary between these structures.

High energy synchrotron X-ray diffraction analysis

To further investigate the microstructure throughout the welded joint, high energy synchrotron X-ray diffraction was performed. For this, a series of diffraction patterns were retrieved from a linear path that encompasses the full extension of the welded joint. The 3D superimposition of the obtained diffraction patterns is presented in Fig. 5a. Here, distinguishing these regions is easily achieved by observing the variation on diffracted intensity of the (111) peak of the γ-FCC phase, as marked.

Figure 5b-d exhibits site specific patterns of the BM, HAZ and FZ, respectively, using a logarithmic scale for intensity, which allows us to observe the low intensity reflections. In all regions the γ-FCC matrix phase is dominant. The BM lattice parameters calculated by fitting each peak and using the intensities as averaging weighting factors was $a_\gamma = 3.6012$ Å (rounded to the fourth decimal). Such value is coherent with that obtained from Rietveld refinement in the same region ($a_\gamma = 3.6018$ Å) and with the lattice parameters found in the literature for similar Fe-based SMA [24, 26–30]. Additionally, Vanadium carbide (VC) peaks, $a_{VC} = 4.1599$ Å, space group: Fm-3 m, are noticeable throughout the BM and HAZ, corresponding to a total phase volume fraction of 0.11%. This phase volume fraction reduces to 0.06% in the FZ, potentially due to the non-equilibrium and faster cooling conditions experienced in this region of the joint. Interestingly, the BM and the HAZ have the same phase structures present within them. Conversely, throughout the FZ (either in the FQZ, columnar or the equiaxed region), the presence of a δ-BCC phase ($a_\delta = 2.8580$ Å, space group: Im-3 m) corresponding to ferrite is also evident, with a phase volume fraction of 1.04%, as well an intermetallic precipitate which occupies a volume fraction of 0.75% on the bulk of the FZ and corresponds to a P2$_1$3 cubic crystal structure ($a_\triangledown = 6.2130$ Å). This allows us to identify the Fe-rich particle scattered within the sub-grains in the FZ TEM samples. As identified in [24], this precipitate is common to find in Fe–Mn–Si–Cr–Ni shape memory alloys, being a Fe$_5$Ni$_3$Si$_2$-type intermetallic isostructural to the π-phase in steels. Such precipitate has also been observed in similar alloys [24, 26, 28, 29, 31]. Nevertheless, the presence of these additional minor intensity phases is only noticeable within the FZ because of the complete localized melting of the material and subsequent non-equilibrium cooling conditions. Concerning
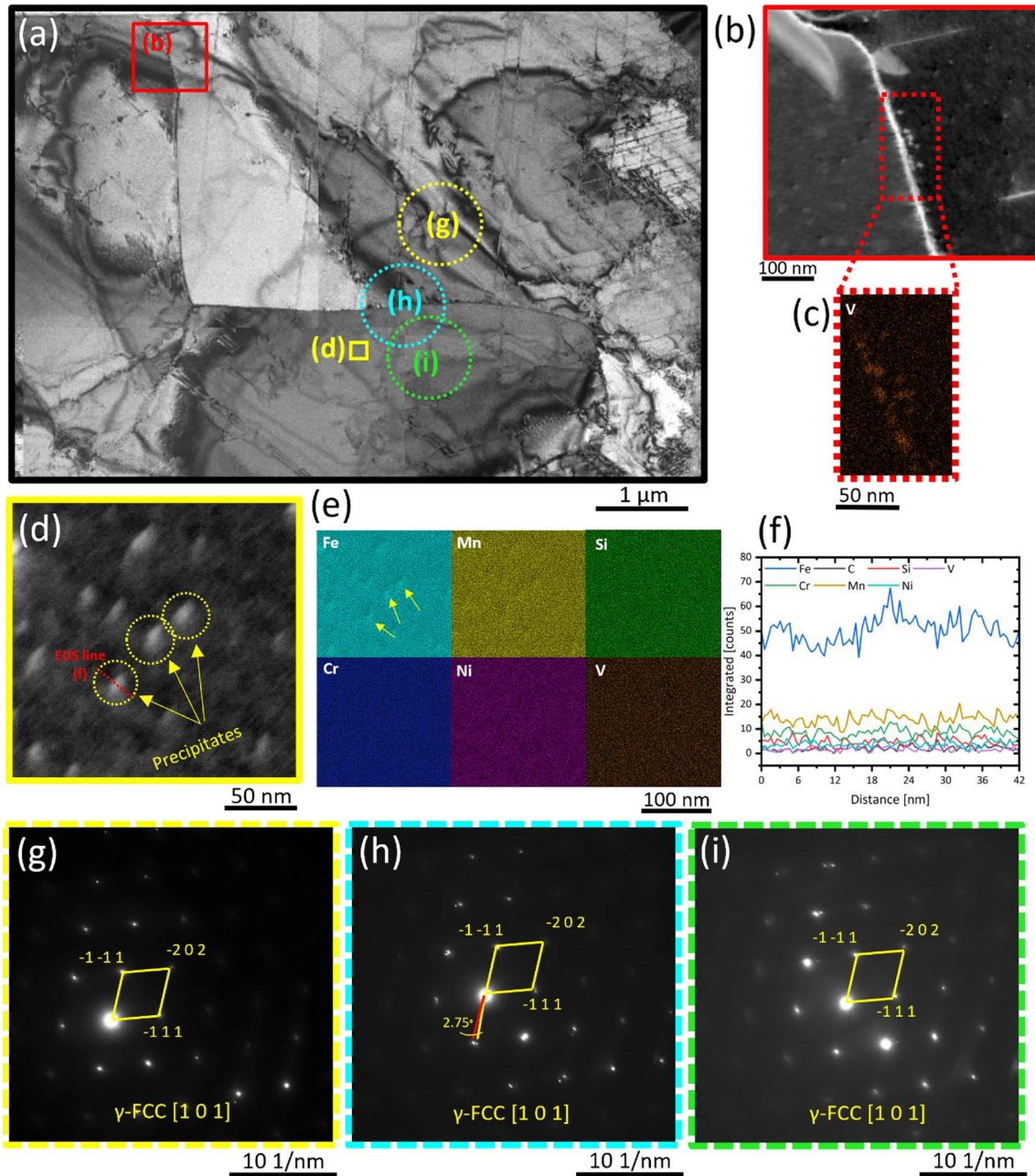
Figure 4 **a** representative bright field TEM image of the FZ; **b** detail of VC precipitates near the sub-grain boundaries, and **c** corresponding EDS map of Vanadium; **d** detail of Fe-rich precipitates scattered withing the sub-grains and corresponding EDS maps in **e** alongside the **f** EDS line results marked in **d**. The transition from one sub-grain to another was inspected using SAED as in **g** upper sub-grain; **h** boundary between sub-grains and **i** lower sub-grain.

the lattice parameters calculated in this region, Rietveld refinement yields an $a_\gamma = 3.6012$ Å, while the peak intensity averaged data results on an $a_\gamma = 3.6014$ Å. Additionally, no indication of the reversible ε-HCP and non-reversible α' phases was found on the joint, as often mentioned in the literature [9, 32–35].

Beyond phase identification and Rietveld refinement for phase quantification, single peak fitting was conducted using an in-house developed python scripts to perform least-squares fitting with a Voight profile, on all the first-order reflections of the matrix γ-FCC phase. This procedure aims to gather data and reveal
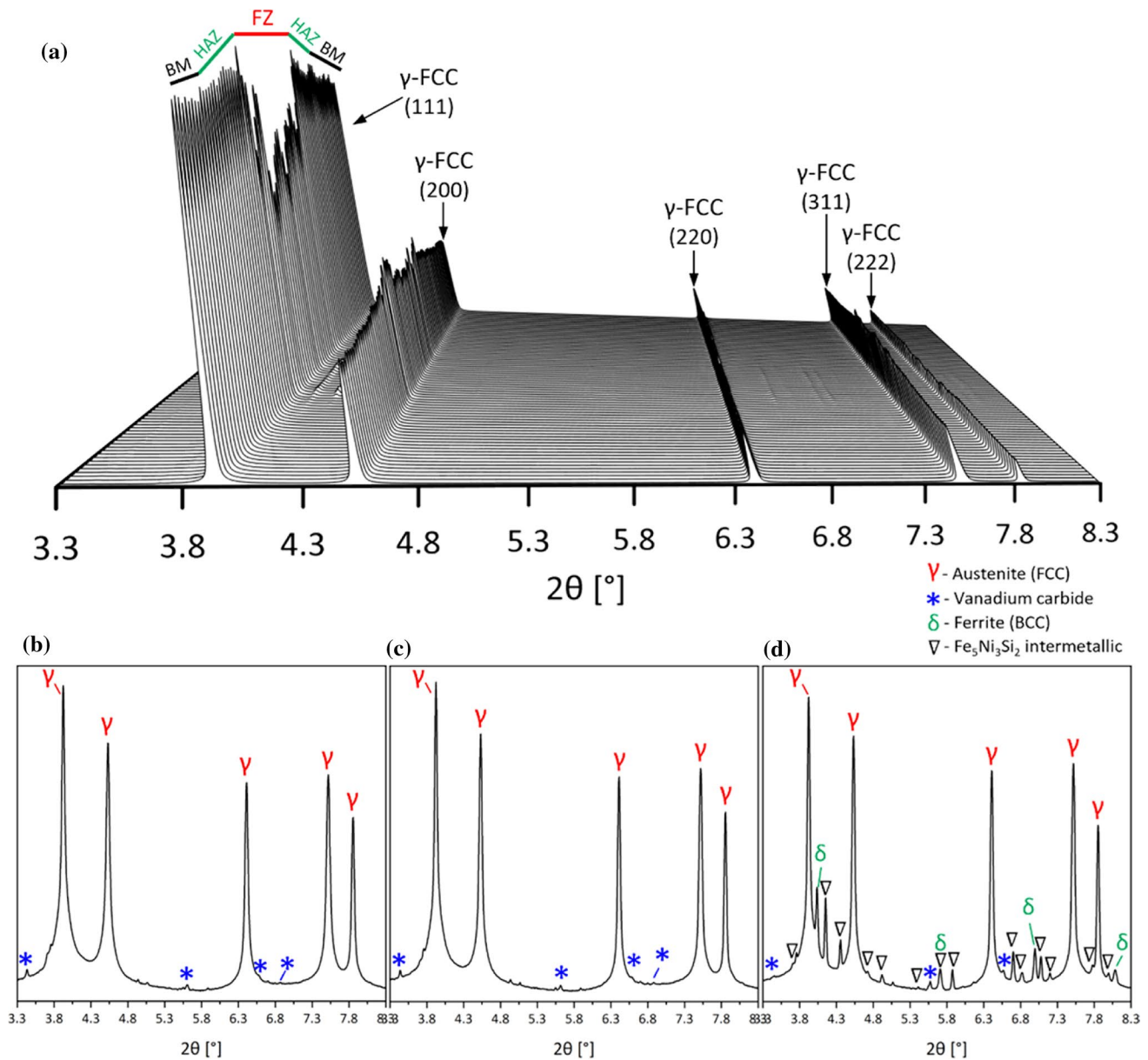
Figure 5 Synchrotron X-ray diffraction patterns taken form **a** the full extension of the weld, highlighting the matrix γ-FCC phase; representative diffraction patterns of: **b** BM, **c** HAZ, **d** FZ, with corresponding phase identification. Low intensity 2nd harmonic diffraction peaks were left unidentified because they do not correspond to any structure present on the alloy.

trends from the intrinsic microstructural phenomena contained within the weld. Here, a qualitative analysis of both the normalized full width at half maximum (FWHM) and intensity can be done conjointly, as displayed in Fig. 6a and b. These values were normalized with respect to the BM.

The FWHM is affected by the microstrain caused by defects within the lattice, and the size of intragranular structures that can diffract light in a coherent manner, as well as by the beamline optics (although this component was removed using LaB_6 calibration powder). The intensity, however, is influenced by texture and volume fraction of each phase within the weld. Nevertheless, both parameters (microstrain and size of the intragranular structures) have a significant impact on the overall shape of the peaks, the only difficulty associated with it being knowing how to interpret them. As such from these two
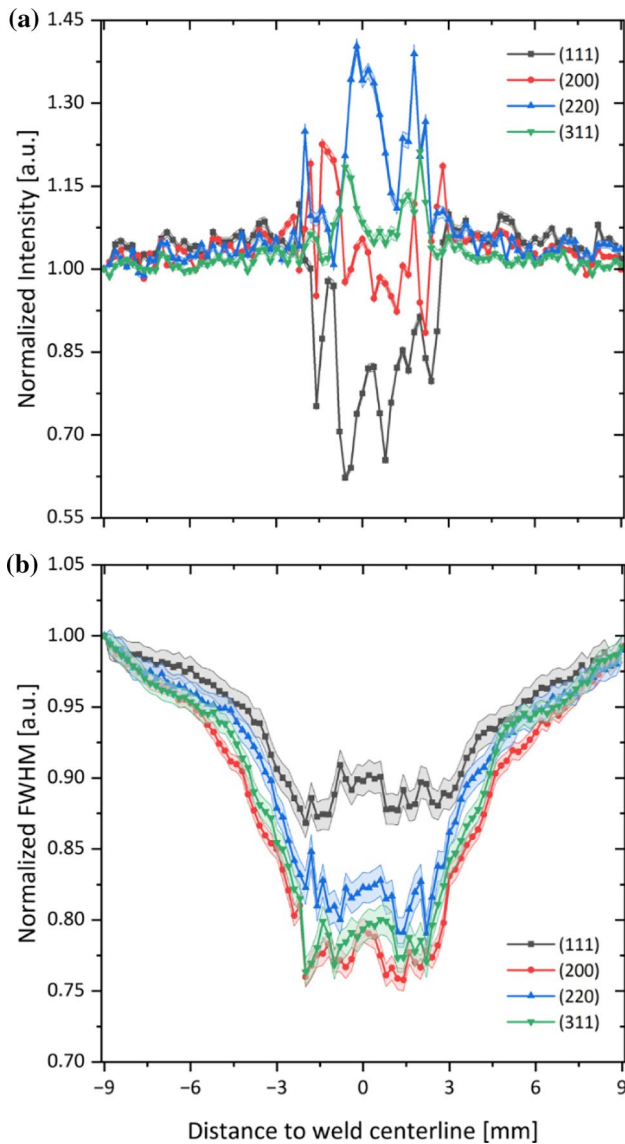
Figure 6 Distribution of **a** peak intensity, and **b** FWHM per diffraction peak along the welded joint.

parameters, one conclusion that can be taken right away is the fact that going towards the FZ, all peaks tend to decrease in FWHM, while increasing in intensity, with exception to the (111) peak. In this case, while the FWHM decreases, the intensity decreases. As mentioned before, this is coherent with the fact the BM is in the as-rolled condition, given that this corresponds to the preferential orientation taken by the grains during deformation. As such, due to high temperatures that cause the material to melt, the texture obtained during the rolling process is annulled, resulting in an overall tendency for its intensity

to decrease. Furthermore, the peak that shows the highest FWHM decrease is the (200) peak, whereas its intensity tends to fluctuate between approx. 0.85 and 1.15 of the value exhibited by the BM, indicating that these diffraction reflections become sharper with proximity to the FZ, which is coherent with the easy growth direction of FCC alloys. Next, we have the (220) reflection, whose intensity increases more than 30% of its intensity on the BM. Such does not quantify the number of grains oriented along the (220) plane, when compared with the (200) oriented grains, but it allows to infer that sharper (220) peaks are present in the FZ, which is related to the crystallographic plane associated with the easy growth direction of the FCC materials [36]. Additionally, of special note is the (311) peak, whose characteristic insensitivity to intergranular strains allows us to highlight the behavior of matrix γ-FCC phase along the welded joint [37]. This is especially, observable in Fig. 6a, where the intensity exhibits an increase near the fusion boundary, corresponding to the FQZ and columnar regions, and finally exhibiting a slight decrease indicating the boundaries of the epitaxial region present in the bulk of the FZ.

Furthermore, quantification of the lattice strain (ε) can be done using (Eq. 2) [38].

$$\varepsilon = \frac{a - a_0}{a_0} \tag{2}$$

where a corresponds to the intensity weighted averaged lattice parameter obtained from all the γ-FCC peaks available on the diffraction patterns. Due to the lack of knowledge of a_0, which corresponds to the strain-free lattice parameter characteristic of this alloy, in this work we set a_0 as the lattice parameter obtained at 0 MPa on the BM. This allows for a still meaningful qualitative assessment of the microstrain evolution, rather than a quantitative evaluation.

Given this, for an understanding of the strain field associated with each zone of interest with sufficient dimensions for a complete acquisition of data given the utilized beam spot size, measurements from the HAZ and columnar and equiaxed regions of the FZ are compared to those obtained from the BM in Fig. 7c, with relation to the azimuthal angle. For such, representative diffraction patterns of each region were integrated into 1-degree segments, allowing to obtain the 2θ center parameter of each peak at any given azimuthal angle segment, where the intensity is sufficient to acquire reliable results.

Figure 7 Comparison between the microstrain of the BM and the: **a** HAZ, **b** columnar region of the FZ and **c** equiaxed region of the FZ.
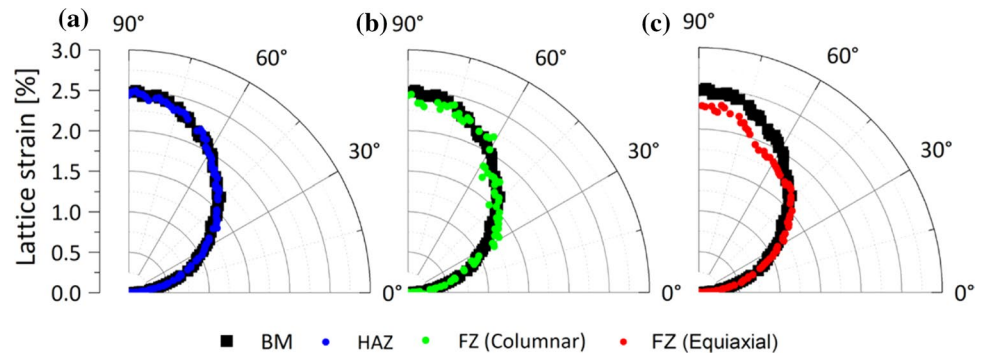
By comparison, all the analyzed regions evidence a similar distribution of microstrain, which is symmetrical on the horizontal and vertical axis. Here the higher macrostrain values are present in the 90° azimuthal angle and the lowest are oriented in the 0° angle. This is coherent with the expected strain conditions considering the as-rolled condition of the BM, where the 90° angle corresponds to the rolling direction and the 0° angle corresponds to the direction normal to it. Interestingly in all regions, including the FZ, where the material underwent total remelting, the microstrain distribution is also higher at the 90° angle when compared to the 0° direction. This allows us to conclude that upon solidification the newly formed grains tend to adjust to the already present microstructure due to epitaxial growth. Thus, causing the lattice parameter evolution to mimic that of the BM, thus granting an approximately isotropic microstrain response throughout the weld.

Additionally, it is also possible to conclude that with increasing distance from the FB the microstrain tends to decrease. Comparing the values obtained in the BM distribution with those expected from the calculated average lattice parameter, the microstrain increases approx. 2.48% in the rolling direction and decreases 0.02% in the 0° direction. On the other extreme, when considering the equiaxed region in the FZ, however, the microstrain is 2.35% higher in the 90° angle and 0.01% lower in the 0° direction.

Up to now a thorough microstructural analysis of the welded joint has been performed. To complement this characterization, an electrochemical comparison of the BM and FZ was performed and these results are presented in the next section. Such was conducted to investigate the corrosion properties of these two regions, allowing us to establish a starting point, from a corrosion-focused electrochemical behavior standpoint, for the design of applications that may rely on welding of this Fe-based SMA.

Electrochemical characterization of the weld

Setting the BM as the benchmark, the corrosion behavior of the weld, namely the FZ (which is region mostly affected by GTAW), was analyzed to attain an understanding of what to expect when exposing such welded material to different environments. These two regions (BM and FZ) correspond to the two microstructural "extremes" on the joint. It is also relevant to mention that for this analysis the FZ was considered in bulk.

For this matter, Fig. 8 displays the anodic polarization curves alongside the corresponding open circuit potential data obtained from the BM and the FZ. Using the Tafel model [39, 40], the corrosion current, I_{corr}, was estimated to be 0.96 mA for the BM and 0.97 mA for the FZ. Although, these values are quite close to each other it is possible to conclude that the corrosion rates of the BM and FZ under the testing conditions were similar, with the FZ exhibiting a slightly lower corrosion resistance that the BM. Nevertheless, interpreting electrochemical results solely based on one parameter may does not capture the entire complexity of the corrosion process.

As such, the EIS measurements performed the BM and the FZ are presented in Fig. 8, in terms Bode and Nyquist diagrams. It can be noted that the impedance modulus, |Z|, of the BM is greater than that of the FZ, corresponding to values up to ≈307 Ω and ≈285 Ω, respectively, at the lowest values of frequency. Regarding the phase angle, for the BM the lower values corresponded to ≈-18.8° at a frequency of ≈20 Hz, while the FZ attained its minimum of ≈-19.7° at a frequency of 12.4 HZ. On the other hand, the maximum phase angle for the BM was ≈ − 1.7° (at a frequency of

Figure 8 Electrochemical characterization of the welded joint ▶ in terms of: **a** polarization curves alongside with the **b** corresponding open circuit potential; **c** Bode plot and corresponding **d** Nyquist plot, obtained on the BM; **e** Bode plot and corresponding **f** Nyquist plot, obtained in the FZ.

≈50.3 kHz), while for the FZ the maximum was ≈-1.4°, recorded at a frequency of ≈15.7 kHz.

While exhibiting a similar corrosion behavior, it can be noted that the BM has a higher corrosion resistance when compared to the FZ, such can be associated to the different microstructural condition of both regions, where the FZ is characterized by varying array of different microstructures.

With this matter established, next we analyze the mechanical properties, correlating them with processing conditions and local microstructure features in order to establish a parallel between the mechanical properties and the obtained microstructure. This highlights the fact that the microstructure not only affects the corrosion behavior of the joint, but also has an important role in its mechanical performance.

Mechanical behavior of the welded joint

Understanding the intricate relationship between microstructure and mechanical properties is paramount when selecting a material for a determined purpose, especially when there is a gradient of microstructures (and therefore of mechanical behavior) in thermomechanically processed material. Having discussed the microstructural aspects that developed within the welded joint, generated by the intense heat imposed during GTAW, in this section we explore the mechanical and functional properties of the joints. Firstly, we start by observing the anisotropic distribution of the microhardness on the weld, followed by the analysis of the tensile and cyclic properties exhibited by it.

Microhardness distribution along the joint

Microhardness maps performed on the full extension of the joint are displayed in Fig. 9. Here, a clear distinction of the regions previously identified in the microstructural section is possible. Interestingly the three regions that comprise the FZ microstructural gradient are again easily identifiable by observing the
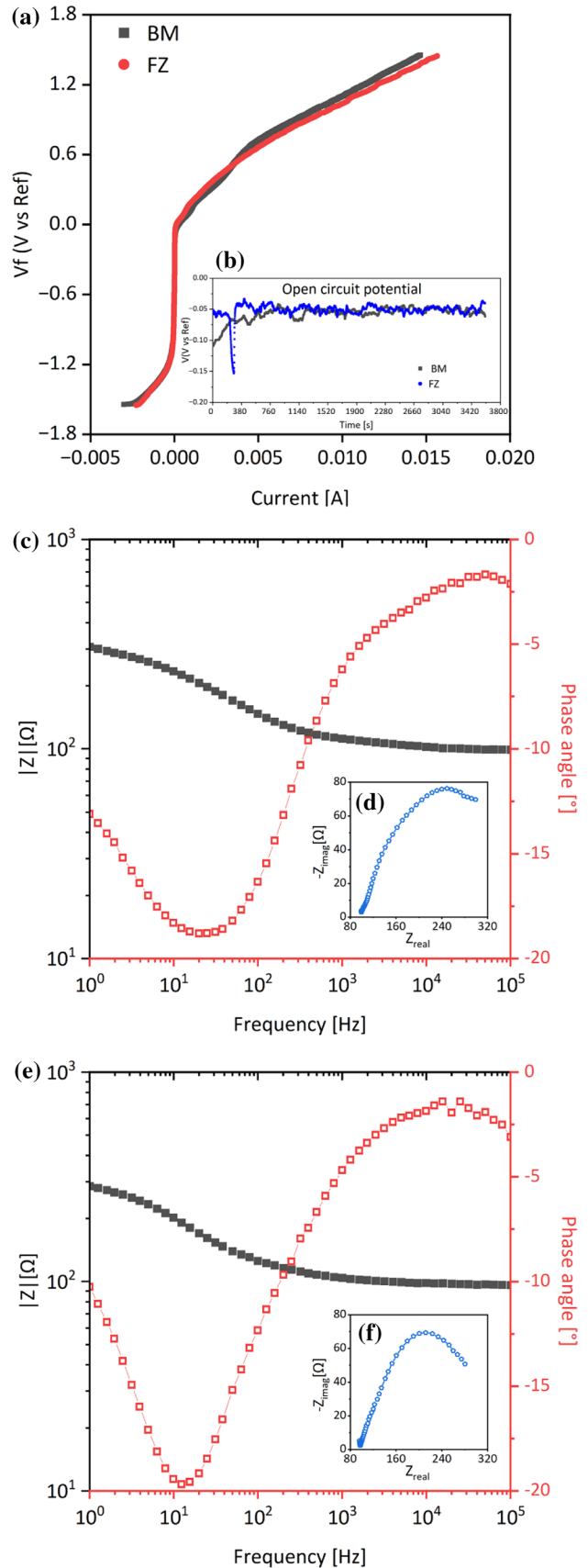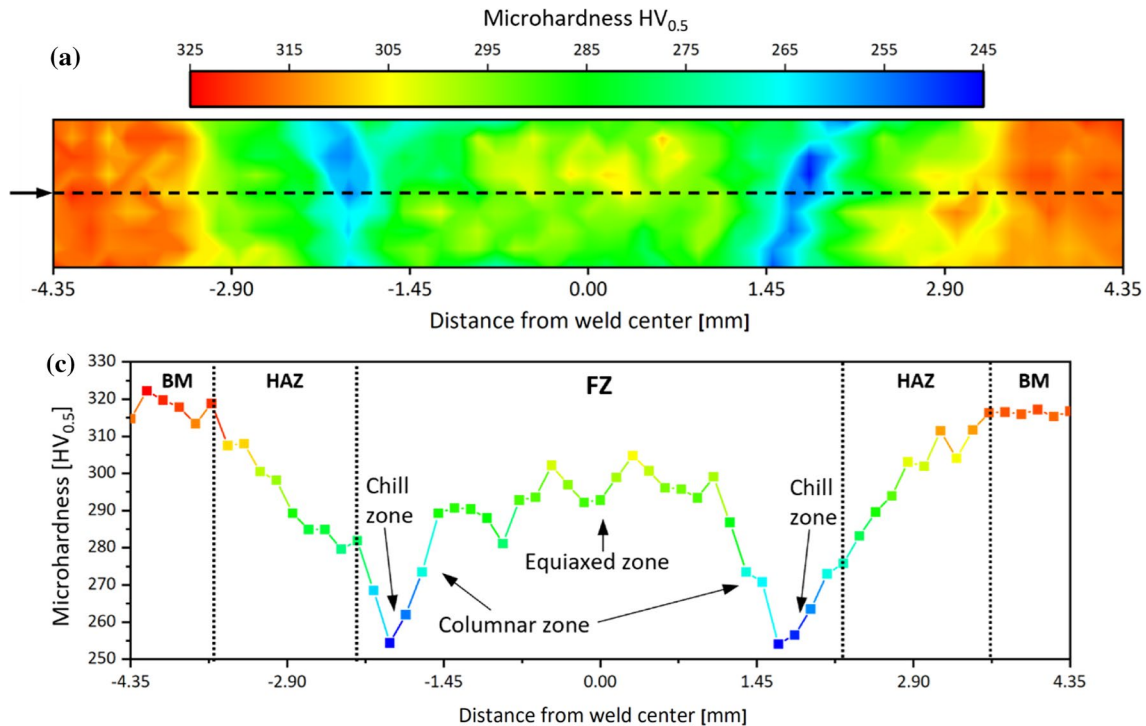
Figure 9 Microhardness distribution of the Fe-SMA welded joint: **a** colormap and **b** evolution at mid height of the weld (marked by the black arrow and dashed line).

FZ microhardness variation. Furthermore, the micro-hardness line data obtained at half height of the cross section of the weld are plotted in Fig. 9b). This also permits us to highlight the microhardness variation between the regions that comprise the welded joint and ease the interpretation of the microhardness map. Here the softening behavior of the chill zone is evident as it marks the region where the weld achieves its lowest microhardness values.

Quantification of the results regarding the micro-hardness distribution along the joint are displayed in Table 1, where the percentual variation of the results of the regions affected by the welding process are compared to the measured BM values. While the BM achieved an averaged microhard-ness corresponding to 316.7 ± 2.9 HV$_{0.5}$, the lowest hardness on the weld was observed in the FQZ of the FZ, reaching 254.5 ± 6.0 HV$_{0.5}$. Concerning the HAZ, the microhardness achieved an average of 286.3 ± 3.8 HV$_{0.5}$. Also, the columnar dendritic and the equiaxed region of the FZ attained the values of 281.5 ± 3.6 HV$_{0.5}$ and 299.0 ± 7.3 HV$_{0.5}$, respectively. This microhardness gradient allows to put in evidence the varying mechanical behavior that the different microstructures induced throughout the weld.

Table 1 Quantification of the microhardness distribution throughout the welded joint microstructure

	BM	HAZ	FZ (Chill zone)	FZ (Columnar zone)	FZ (Equiaxed zone)
Micro-hardness [HV$_{0.5}$]	316.7 ± 2.9	286.3 ± 3.8	254.5 ± 6.0	281.5 ± 3.6	299.0 ± 7.3
Percentual deviation from the BM	–	-9.6%	-19.6%	-11.1%	-5.6%

Tensile properties of the welds coupled with digital image correlation (DIC)

With the microhardness distribution determined, an obvious anisotropic distribution of the microstructure and its impact on the local mechanical response is clear. Given this, the next step is to analyze the tensile behavior of the welded joint, to highlight the mechanical performance differences that arise from the microstructural changes developed in the HAZ and FZ.
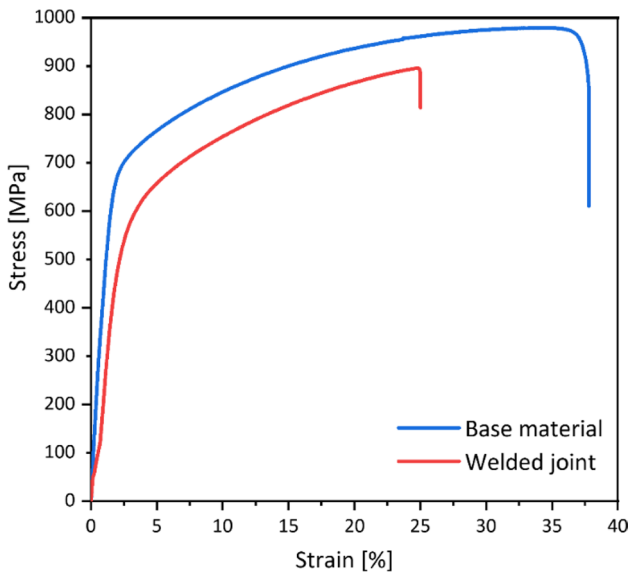

Figure 10 Representative stress–strain curves of the **a** base material and **b** welded joint, taken from the multiple tensile tests performed on the samples (three in each condition).

The representative stress–strain curves of the BM and welded joint are plotted in Fig. 10.

Overall, the obtained tensile test data indicates that regarding the ultimate tensile strength (UTS), the BM samples achieved 1032.9 ± 76.3 MPa, while the welds reached an averaged UTS of 883 ± 18.4 MPa, corresponding to fracture strains of $36.8 \pm 1.5\%$ and $23.6 \pm 2.1\%$ (all engineering values), respectively. This indicates that the welds retained 85.5% of the UTS exhibited by the BM, reaching 64.1% of the strain-to-fracture exhibited by it. The UTS values show a good agreement with those found in the literature [18, 41–43], while the elongation to fracture tends to vary accordingly with the thermomechanical treatment they are subjected to.

It can be concluded that the tensile strength evidences a small decrease when comparing the welds with the BM, while the ductility deteriorated more severely after the GTAW process. This, as seen through the microhardness measurements, can be related to the varying microstructural features arising from the solidification of the molten pool and consequent inhibition of the overall strength of the BM imposed by rolling process. Furthermore, the presence of δ-BCC ferrite and the ∇-precipitate phases can also explain the different tensile behavior exhibited by the welded samples. Nonetheless, the overall macroscopic mechanical behavior of these Fe-based SMAs make them suitable candidates for structural engineering application scenarios.

Under the effect of a constant tensile force imposed on the joints, the data regarding the mechanical

Figure 11 Depiction of the strain distribution during tensile testing in the as-welded condition, using digital image correlation: **a** corresponds to the evolution until fracture, while in **b** the last stage before fracture is depicted on a different scale. The regions marked in **b** are utilized to plot the local tensile behavior in Fig. 12.
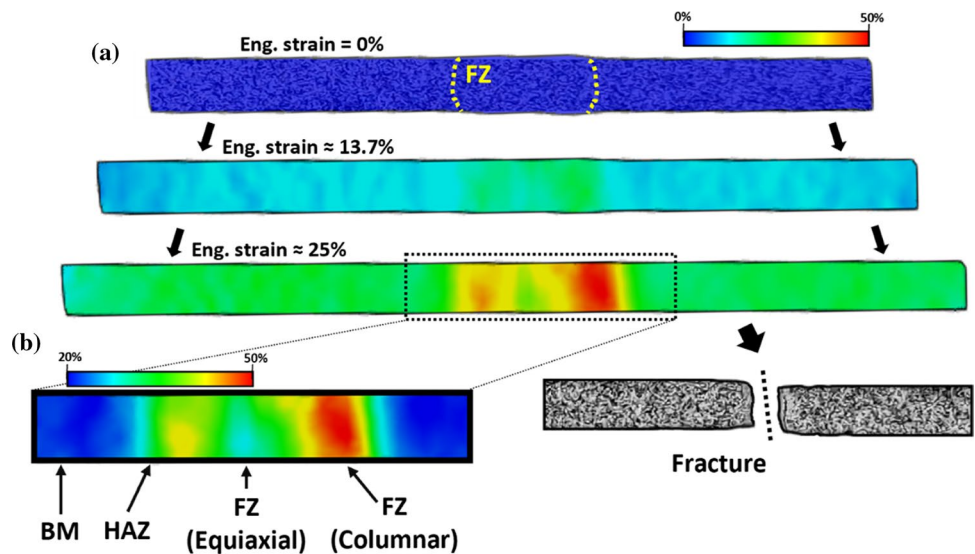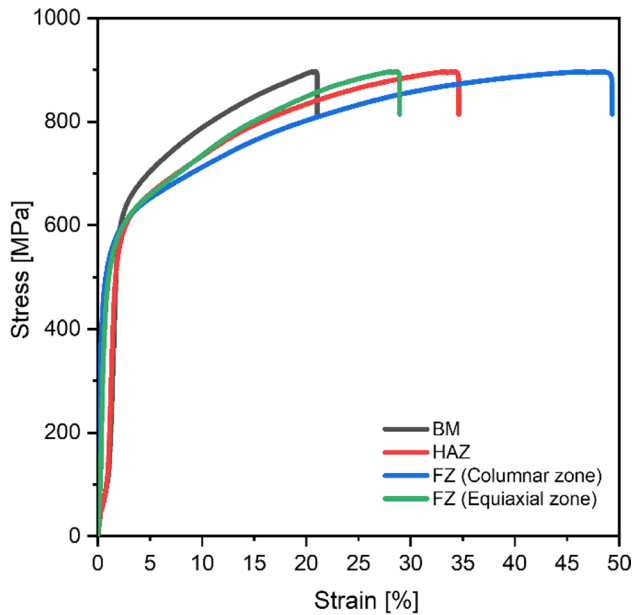
Figure 12 DIC results for the BM, HAZ and two region (columnar and equiaxed) zones of the FZ.

behavior of the welds corresponds to the combined behavior of all regions of the weld. For this reason, to further evaluate the microscopic tensile behavior exhibited by each welded region, DIC data was

recorded during tensile testing and specific locations were monitored to evaluate their site-specific behavior. The strain distribution results during tensile testing are displayed in Fig. 11. Here the evolution of the strain distribution along the welded joint is shown, clearly indicating that more deformation occurred in the GTAW affected area than in the BM itself.

As expected, from the start of the tensile test until sample fracture, an increase in strain is observed as can be seen through the color distribution at the displayed engineering strain values. By inspecting the last moments of the tensile test (see Fig. 11b), it is possible to observe that the variating microstructure present within the samples indeed has an important effect on the overall strain that is accommodated by each region of the weld. By direct observation, it is possible to observe that while the BM was the region where less strain was accumulated, the columnar zone of the FZ presents itself with the most amount of strain. Interestingly the equiaxed zone located at the middle of the FZ (refer to Fig. 1) exhibits a higher resistance to the imposed stress. This was expected considering the refined morphology of the grains in this region and the associated higher microhardness. Thus, this equiaxed microstructure present in the equiaxed zone is preferred over the other microstructures existing in the FZ of the weld. For further analysis Fig. 12 displays

Figure 13 Representative fracture surface of the welded samples.
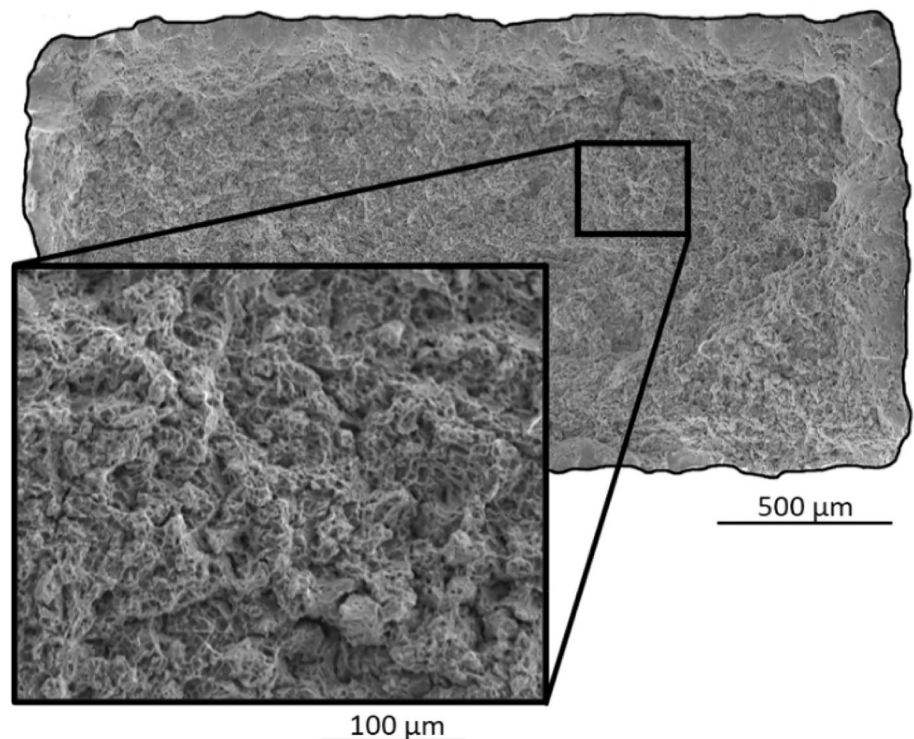
the stress–strain curves calculated considering specific regions of the weld, as mentioned, and a clear distinction and quantification of the strain experienced by each region is presented.

Qualitatively, it can be observed that the BM and the equiaxed zone in FZ, exhibited a lower amount of deformation upon loading. While both are characterized by their small grain size and higher microhardness which grants them strength, another factor influencing their behavior is the deformed state of the BM (which hinder dislocation movement) and the occurrence of precipitates in the FZ.

These regions are followed by the HAZ which experienced grain growth during the welding process and is composed of large equiaxed grains. Finally, the region with the most amount of deformation experienced is the columnar region of the FZ, which reaches similar microhardness values to the HAZ but has larger and highly oriented grains. Nevertheless, as necking started to occur on the sample it was clearly observed that the samples fractured on the interface between the FZ and the HAZ, presumably in the chill zone given its lower values of microhardness.

To better understand the fracture mechanisms that occurred during tensile testing, a SEM image of the post-fracture surface is exhibited in Fig. 13. There, it is possible to observe several dimples which are characteristic of a ductile-like fracture upon tensile solicitation. That is, as the material is exposed to a plastic deformation, small voids and cavities tend to form inside the material. These eventually grow larger and coalesce into each other, forming fissures that propagate perpendicularly to the stress direction, especially in the peripheral zone of the region that experiences necking.

Weld performance under cycling tests

To further understand the mechanical/functional response of this Fe–Mn–Si–Cr–Ni SMA in the as-welded condition, samples were subjected to a routine of load/unload cycles to investigate parameters such as absorbed energy and accumulated irrecoverable strain. Figure 14 presents the stress–strain curves corresponding to the 1st, 2nd, 10th, 25th, 50th, 75th and 100th loading cycles on both the welded and non-welded (BM) conditions. By comparison, it is evident that in both cases the curves display a small pseudoplastic behavior, showcasing slightly lower stress
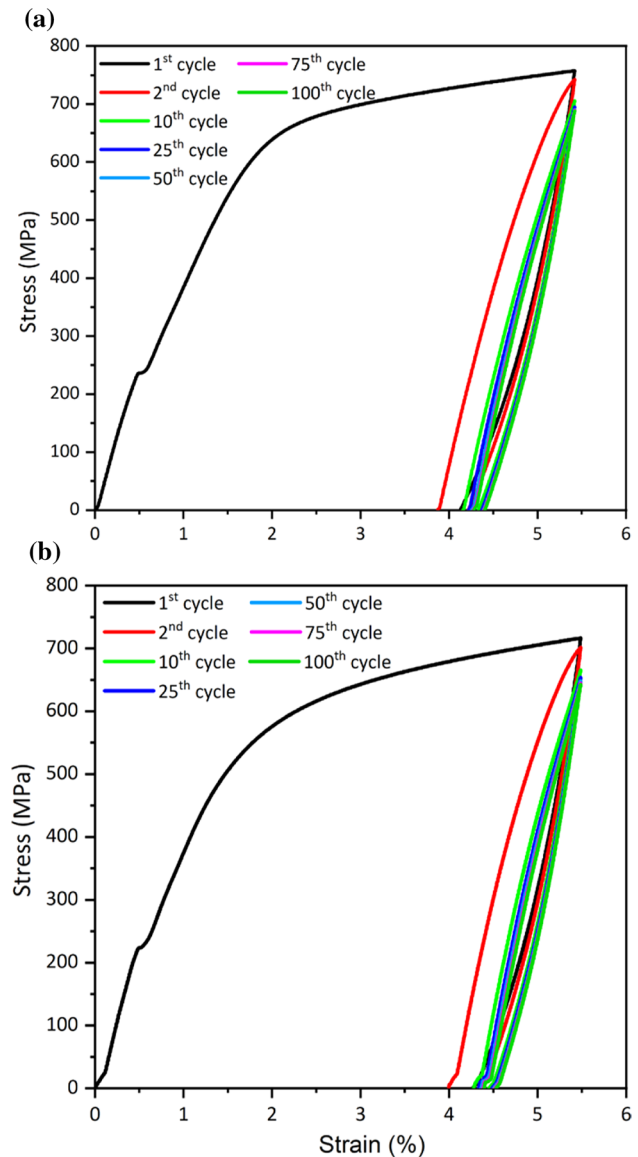

**Figure 14** Load/unload cycling tests performed on: **a** BM and **b** welded samples.

and strain values on the as-welded condition. In both cases, the first cycle possesses a large hysteresis loop, however, as more cycles are completed, the presence of cycle hardening becomes evident due to the occurrence of plastic deformation that degrades the reversibility of the phase transformation.

Figure 15 details the evolution of irrecoverable strain, maximum strain and absorbed energy during the 100 load/unload cyclic tests performed. By comparison, it can be observed that in the as-welded condition the percentage of unrecoverable strain exhibits a slight increasing slope after the 20th cycle, while

Figure 15 Results from cycling tests: **a** Irrecoverable strain; **b** ▶ maximum stress at 6% strain and **c** absorbed energy.

the BM samples appears to become constant, indicating the start of a functional fatigue in the welded condition. This can be explained by the fact that by the end of each cycle, dislocations and defects start to accumulate throughout the various regions that compose a weld. This behavior is further compounded by the non-uniform microstructure of the joint which renders a preferential plastic deformation to occur, rather than a homogenous distribution as it occurs in the BM. Furthermore, the behavior highlighted by the irrecoverable strain curves indicate the development of a ratcheting behavior, which is typical in stress-controlled cycling and was also observed in [18, 44]. As explained by Koster et al. [18], the superelastic behavior that this alloy exhibits, occurs due to the low stacking fault energy of the Fe-based SMAs, which provides the means for Shockley partial dislocations to occur and shift easily throughout the austenitic microstructure upon loading. Such process generates stacking faults and induces the martensitic transformation on the alloy. In this particular composition, the VC precipitates alongside the grain boundaries act as barriers to the movement of dislocations, promoting localized stresses in the newly formed martensitic phase. Conversely, during the unloading cycles this accumulated stress is released, pushing the Shockley partial dislocations in a reverse movement, resulting in the reverse transformation of the martensite back to austenite, and consequently causing the partial recovery of strain.

Figure 15b displays the maximum stress for an imposed strain of 6%, obtained from the BM and welded joints at each cycle. As it is possible to observe in both curves, there is a sharp decrease in slope up to the 20th cycle, after which the curves exhibit a steadier decrease in value, with the BM case showcasing a minor tendency for further decrease, stabilizing at approximately 690 MPa. Considering the difference from the beginning of the cycling test to the 100th cycle, the BM exhibits a decrease of 69 MPa, while the weld exhibits a decrease of a total of 74 MPa. In comparison to the BM, this behavior indicates that in the as-welded case a slightly higher functional fatigue can be noted, possibly due to the varying microstructural features that were previously highlighted and are presented along the welded joint. This factor may ease the conditions for the continuous formation of
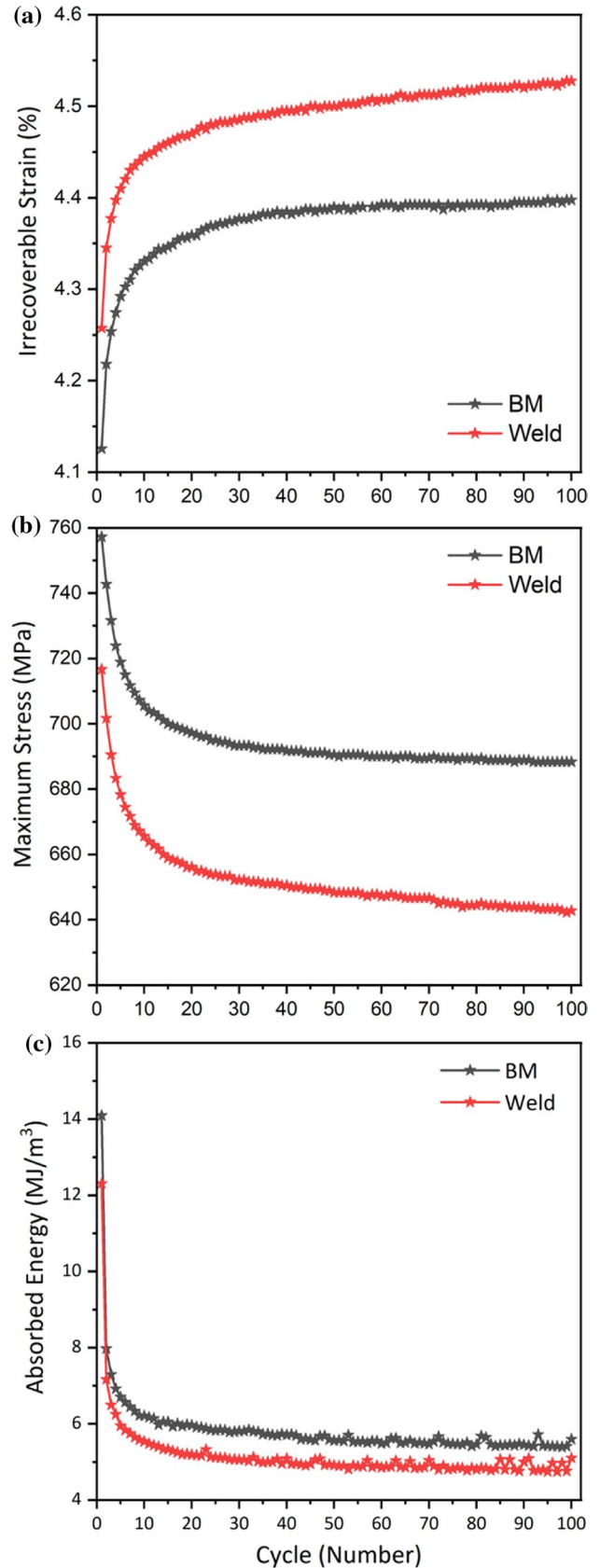
microstructural defects, developed on the larger grains on the HAZ or on the varying dendritic structures in the FZ, easing stress accommodation at each loading step. Similar conclusions on the maximum stress analysis were also reported in [18, 41], although using different testing parameters and with prior thermal activation of the SMA.

Furthermore, the amount of absorbed energy upon each cycle is also a relevant property for any engineering applications operating under dynamical loading. The results exhibited by the welded SMA and BM counterpart for this property are shown in Fig. 15c. As it is possible to observe, the first cycles are characterized by the stabilization of the superelastic hysteresis, where a sudden decline on the absorbed energy can be seen in the behavior of both samples. Here the difference between the first two cycles was approximately 6.12 MJ/m^3 in the BM and 5.14 MJ/m^3 in the weld. Further on, with the increasing number of cycles, the behavior exhibited by both samples presents several similarities, with the welded joint absorbing a slightly lower amount of energy throughout the tests. This can be attributed to the inhomogeneous microstructure of the welded joint. Nevertheless, a decrease of approximately 2.38 MJ/m^3 and 2.06 MJ/m^3 from the 2nd cycle to the 100th can be observed in the BM and welded joints, respectively. This indicates a low functional fatigue in both cases, given the relatively constant energy absorption after the 2nd cycle.

Conclusions

"In this study, the weldability of an Fe–Mn–Si–Cr–Ni SMA was assessed by means of conventional and advanced microstructural techniques coupled with mechanical characterization. Thorough analysis via optical and electron microscopy revealed the formation of an FQZ, a columnar and an equiaxial within the fusion zone of the joint. Beyond these, the formation of a HAZ was also evident, arising from the thermal impact induced by the high temperatures attained during welding.

Further advanced characterization using TEM and synchrotron X-ray diffraction evidence local, micro and nanoscale differences within the welded joint. Such allowed to identify not only a Fe$_5$Ni$_3$Si$_2$-type intermetallic with a P2$_1$3 cubic crystal structure, within the bulk of the FZ, but also the presence of vanadium carbides dispersed amidst the matrix austenitic phase.

Arising from the effect of the high temperatures and solidification modes on the FZ, a ferritic phase was also noticed.

On a practical perspective, electrochemical characterizations were performed revealing that the BM is less prone to corrosion than the FZ, which requires care upon the use of these joints in corrosive media. The obtained impedance modulus was ≈307 Ω for the BM and ≈285 Ω for the FZ. Furthermore, microhardness mapping on the joint permitted to quantify the hardness at each weld region, where the maximum values were obtained in the BM, corresponding to 316.7 ± 2.9 HV$_{0.5}$. The lowest microhardness values, corresponding to 254 ± 6 HV$_{0.5}$, were observed in the chill zone of the FZ.

Upon tensile testing, a maximum strength of 883 ± 18.4 MPa was achieved on the welded joints, with a fracture strain of 23.6 ± 2.1%. Such values correspond to 85.5 and 64.1% of the tensile response of the BM, respectively. Coincidental with the tensile test data, DIC analysis revealed a different mechanical response between the difference regions of the joint, which was correlated with the associated microstructure features. Such was especially noticeable in the FZ, where the most ductile region was the columnar zone, while the equiaxed region exhibited a lower ductility. Upon fracture, post-mortem surface analysis indicated that ductile failure occurred. Finally, functional fatigue testing was conducted revealing, that cyclic degradation was slightly exacerbated in the welded joint due to the inhomogeneous microstructure that developed across the thermally affected regions.

Overall, defect-free welds were obtained on the studied Fe–Mn–Si–Cr–Ni SMA, indicating that it can be a viable solution for structural applications as good mechanical properties were achieved. Such showcases the potential use of GTAW on this advanced SMA in different industrial settings. Future works may envisage studying the dissimilar weldability of this SMA.

Acknowledgements

Author contributions

JGL Conceptualization, Data curation, Formal analysis, Investigation, Writing—original draft. DM Data curation, Formal analysis, Investigation. KZ Data curation, Investigation. BL Data curation, Investigation. BW Investigation. XW Data curation, Investigation. NS Data curation, Investigation. EG Investigation, Writing—review & editing. ACB Data curation, Investigation. JPO Formal analysis, Resources, Project administration, Supervision, Writing—review & editing.

Funding

Open access funding provided by FCT|FCCN (b-on).

Data availability

Data will be available upon request.

Declarations

Conflict of interest   The authors declare that they have no conflict of interest.

Ethical approval   Not Applicable.

References

[1] Izadi MR, Ghafoori E, Shahverdi M, Motavalli M, Maalek S (2018) Development of an iron-based shape memory alloy (Fe-SMA) strengthening system for steel plates. Eng Struct. https://doi.org/10.1016/j.engstruct.2018.07.073

[2] Czaderski C, Shahverdi M, Michels J (2021) Iron based shape memory alloys as shear reinforcement for bridge girders. Constr Build Mater. https://doi.org/10.1016/j.conbuildmat.2020.121793

[3] Izadi MR, Ghafoori E, Motavalli M, Maalek S (2018) Iron-based shape memory alloy for the fatigue strengthening of cracked steel plates: Effects of re-activations and loading frequencies. Eng Struct 176:953–967. https://doi.org/10.1016/J.ENGSTRUCT.2018.09.021

[4] Hosseini E, Ghafoori E, Leinenbach C, Motavalli M, Holdsworth SR (2018) Stress recovery and cyclic behaviour of an Fe–Mn–Si shape memory alloy after multiple thermal activation. Smart Mater Struct 27:025009. https://doi.org/10.1088/1361-665X/AAA2C9

[5] Druker AV, Perotti A, Esquivel I, Malarría J (2014) A manufacturing process for shaft and pipe couplings of Fe–Mn–Si–Ni–Cr shape memory alloys. Mater Design (1980–2015) 56:878–888. https://doi.org/10.1016/J.MATDES.2013.11.032

[6] Kanayo Alaneme K, Anita Okotete E (2016) Reconciling viability and cost-effective shape memory alloy options-a review of copper and iron based shape memory metallic systems. Eng Sci Technol Int J. https://doi.org/10.1016/j.jestch.2016.05.0103

[7] Ferretto I, Kim D, Della Ventura NM, Shahverdi M, Lee W, Leinenbach C (2021) Laser powder bed fusion of a

Fe-Mn-Si shape memory alloy. Addit Manuf 46:102071. https://doi.org/10.1016/j.addma.2021.102071

[8] Vůjtěch J, Ryjáček P, Campos Matos J, Ghafoori E (2021) Iron-Based shape memory alloy for strengthening of 113-Year bridge. Eng Struct. https://doi.org/10.1016/j.engstruct.2021.113231

[9] Cladera A, Weber B, Leinenbach C, Czaderski C, Shahverdi M, Motavalli M (2014) Iron-based shape memory alloys for civil engineering structures: an overview. Constr Build Mater 63:281–293. https://doi.org/10.1016/J.CONBUILDMAT.2014.04.032

[10] Sawaguchi T, Nikulin I, Ogawa K, Sekido K, Takamori S, Maruyama T, Chiba Y, Kushibe A, Inoue Y, Tsuzaki K (2014) Designing Fe-Mn-Si alloys with improved low-cycle fatigue lives. Scripta Mater. https://doi.org/10.1016/j.scriptamat.2014.11.024

[11] Deng W, Wang C, Lu H, Meng X, Wang Z, Lv J, Luo K, Lu J (2023) Progressive developments, challenges and future trends in laser shock peening of metallic materials and alloys: a comprehensive review. Int J Mach Tools Manuf 191:104061. https://doi.org/10.1016/J.IJMACHTOOLS.2023.104061

[12] Kou S (2002) Welding metallurgy. Weld Metall. https://doi.org/10.1002/0471434027

[13] Huang W, Cai W, Rinker TJ, Bracey J, Tan W (2023) Effects of laser oscillation on metal mixing, microstructure, and mechanical property of Aluminum-Copper welds. Int J Mach Tools Manuf 188:104020. https://doi.org/10.1016/J.IJMACHTOOLS.2023.104020

[14] Chen CM, Kovacevic R (2004) Joining of Al 6061 alloy to AISI 1018 steel by combined effects of fusion and solid state welding. Int J Mach Tools Manuf 44:1205–1214. https://doi.org/10.1016/J.IJMACHTOOLS.2004.03.011

[15] Nagira T, Nakamura T, Yoshinaka F, Sawaguchi T, Aoki Y, Kamai M, Fujii H, Takeuchi A, Uesugi M (2022) Direct observation of solidification behaviors of Fe-Mn-Si alloys during TIG spot welding using synchrotron X-ray. Scr Mater 216:114743. https://doi.org/10.1016/j.scriptamat.2022.114743

[16] Ju H, Lin C, Liu Z, Zhang J (2018) Study of in-situ formation of Fe-Mn-Si shape memory alloy welding seam by laser welding with filler powder. Opt Laser Technol 104:65–72. https://doi.org/10.1016/J.OPTLASTEC.2018.01.062

[17] Lin HC, Lin KM, Chuang YC, Chou TS (2000) The welding characteristics of Fe–30Mn–6Si and Fe–30Mn–6Si–5Cr shape memory alloys. J Alloys Compd 306:186–192. https://doi.org/10.1016/S0925-8388(00)00762-3

[18] Koster M, Lee WJ, Schwarzenberger M, Leinenbach C (2015) Cyclic deformation and structural fatigue behavior of an FE–Mn–Si shape memory alloy. Mater Sci Eng, A 637:29–39. https://doi.org/10.1016/J.MSEA.2015.04.028

[19] Toby BH, Von Dreele RB (2013) GSAS-II: the genesis of a modern open-source all purpose crystallography software package. J Appl Crystallogr 46:544–549. https://doi.org/10.1107/S0021889813003531

[20] Hu YN, Wu SC, Chen L (2019) Review on failure behaviors of fusion welded high-strength Al alloys due to fine equiaxed zone. Eng Fract Mech 208:45–71. https://doi.org/10.1016/J.ENGFRACMECH.2019.01.013

[21] Shao Y, Li X, Chen L, He E (2022) New insights into fine equiaxed zone of laser-welded 2A97 Al-Li alloy. J Alloys Compd 895:162717. https://doi.org/10.1016/J.JALLCOM.2021.162717

[22] Rajasekhar K, Harendranath CS, Raman R, Kulkarni SD (1997) Microstructural evolution during solidification of austenitic stainless steel weld metals: a color metallographic and electron microprobe analysis study. Mater Charact 38:53–65. https://doi.org/10.1016/S1044-5803(97)80024-1

[23] Peng H, Wen Y, Du Y, Chen J, Yang Q (2014) A new set of Creq and Nieq equations for predicting solidification modes of cast austenitic Fe-Mn-Si-Cr-Ni shape memory alloys. Metall Mater Trans B: Process Metall Mater Process Sci 45:6–11. https://doi.org/10.1007/S11663-013-0005-8

[24] Fuster V, Druker AV, Baruj A, Malarría J, Bolmaro R (2015) Characterization of phases in an Fe–Mn–Si–Cr–Ni shape memory alloy processed by different thermomechanical methods. Mater Charact 109:128–137. https://doi.org/10.1016/J.MATCHAR.2015.09.026

[25] Druker A, La Roca P, Vermaut P, Ochin P, Malarría J (2012) Microstructure and shape memory properties of Fe–15Mn–5Si–9Cr–5Ni melt-spun ribbons. Mater Sci Eng, A 556:936–945. https://doi.org/10.1016/J.MSEA.2012.07.097

[26] Maji BC, Krishnan M, Verma A, Basu R, Samajdar I, Ray RK (2015) Effect of pre-straining on the shape recovery of Fe-Mn-Si-Cr-Ni shape memory alloys. Metall Mater Trans A Phys Metall Mater Sci 46:639–655. https://doi.org/10.1007/S11661-014-2645-Y

[27] Kirindi T, Güler E, Dikici M (2007) Effects of homogenization time on the both martensitic transformations and mechanical properties of Fe–Mn–Si–Cr–Ni shape memory alloy. J Alloys Compd 433:202–206. https://doi.org/10.1016/J.JALLCOM.2006.06.091

[28] Maji BC, Krishnan M, Gouthama, Ray RK (2011) Role of Si in improving the shape recovery of FeMnSiCrNi shape memory alloys. Metall Mater Trans A Phys Metall Mater Sci. 42:2153–2165. https://doi.org/10.1007/S11661-011-0651-X

[29] Maji BC, Krishnan M (2013) Effect of copper addition on the microstructure and shape recovery of Fe–Mn–Si–Cr–Ni shape memory alloys. Mater Sci Eng, A 570:13–26. https://doi.org/10.1016/J.MSEA.2013.01.061

[30] Malamud F, Guerrero LM, La Roca P, Sade M, Baruj A (2018) Role of Mn and Cr on structural parameters and strain energy during FCC-HCP martensitic transformation in Fe-Mn-Cr shape memory alloys. Mater Des 139:314–323. https://doi.org/10.1016/J.MATDES.2017.11.017

[31] Maji BC, Krishnan M (2003) The effect of microstructure on the shape recovery of a Fe–Mn–Si–Cr–Ni stainless steel shape memory alloy. Scr Mater 48:71–77. https://doi.org/10.1016/S1359-6462(02)00348-2

[32] Pan MM, Zhang XM, Zhou D, Misra RDK, Chen P (2020) Fe–Mn–Si–Cr–Ni based shape memory alloy: thermal and stress-induced martensite. Mater Sci Eng, A 797:140107. https://doi.org/10.1016/J.MSEA.2020.140107

[33] Jang WY, Gu Q, Van Humbeeck J, Delaey L (1995) Microscopic observation of γ-phase and ε- and α′-martensite in Fe Mn Si-based shape memory alloys. Mater Charact 34:67–72. https://doi.org/10.1016/1044-5803(94)00054-O

[34] Khodaverdi H, Mohri M, Ghafoori E, Ghorabaei AS, Nili-Ahmadabadi M (2022) Enhanced pseudoelasticity of an Fe–Mn–Si-based shape memory alloy by applying microstructural engineering through recrystallization and precipitation. J Market Res 21:2999–3013. https://doi.org/10.1016/J.JMRT.2022.10.092

[35] Mohri M, Ferretto I, Leinenbach C, Kim D, Lignos DG, Ghafoori E (2022) Effect of thermomechanical treatment and microstructure on pseudo-elastic behavior of Fe–Mn–Si–Cr–Ni-(V, C) shape memory alloy. Mater Sci Eng, A 855:143917. https://doi.org/10.1016/J.MSEA.2022.143917

[36] Lopes JG, Agrawal P, Shen J, Schell N, Mishra RS, Oliveira JP (2023) Evolution of microstructure and mechanical properties in gas tungsten arc welded dual-phase $Fe_{50}Mn_{30}Co_{10}Cr_{10}$ high entropy alloy. Mater Sci Eng, A 878:145233. https://doi.org/10.1016/J.MSEA.2023.145233

[37] Oliveira JP, Curado TM, Zeng Z, Lopes JG, Rossinyol E, Park JM, Schell N, Braz Fernandes FM, Kim HS (2020) Gas tungsten arc welding of as-rolled CrMnFeCoNi high entropy alloy. Mater Des. https://doi.org/10.1016/j.matdes.2020.108505

[38] Song C, Yu H, Lu J, Zhou T, Yang S (2018) Stress partitioning among ferrite, martensite and retained austenite of a TRIP-assisted multiphase steel: an in-situ high-energy X-ray diffraction study. Mater Sci Eng, A 726:1–9. https://doi.org/10.1016/J.MSEA.2018.04.066

[39] Flitt HJ, Schweinsberg DP (2005) Evaluation of corrosion rate from polarisation curves not exhibiting a Tafel region. Corros Sci 47:3034–3052. https://doi.org/10.1016/J.CORSCI.2005.06.014

[40] Barauskienė I, Laukaitis G, Valatka E (2023) Stainless steel as an electrocatalyst for overall water splitting under alkaline and neutral conditions. J Electroanal Chem 950:117880. https://doi.org/10.1016/J.JELECHEM.2023.117880

[41] Ghafoori E, Hosseini E, Leinenbach C, Michels J, Motavalli M (2017) Fatigue behavior of a Fe-Mn-Si shape memory alloy used for prestressed strengthening. Mater Des 133:349–362. https://doi.org/10.1016/J.MATDES.2017.07.055

[42] Rosa DIH, Hartloper A, de Castro e Sousa A, Lignos DG, Motavalli M, Ghafoori E (2021) Experimental behavior of iron-based shape memory alloys under cyclic loading histories. Constr Build Mater. 272:121712. https://doi.org/10.1016/J.CONBUILDMAT.2020.121712

[43] Gu X-L, Chen Z-Y, Yu Q-Q, Ghafoori E (2021) Stress recovery behavior of an Fe-Mn-Si shape memory alloy. Eng Struct. https://doi.org/10.1016/j.engstruct.2021.112710

[44] Paul SK (2019) A critical review of experimental aspects in ratcheting fatigue: microstructure to specimen to component. J Market Res 8:4894–4914. https://doi.org/10.1016/J.JMRT.2019.06.014